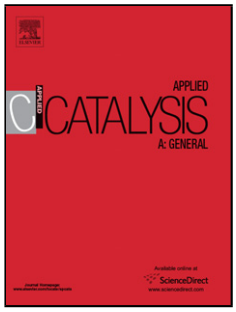

Unraveling mechanistic aspects of the total oxidation of methane over Mn, Ni and Cu spinel cobaltites via *in situ* electrical conductivity measurements

Marius-Alexandru Mihai, Daniela Cristina Culita, Irina Atkinson, Florica Papa, Ionel Popescu, Ioan-Cezar Marcu

PII: S0926-860X(20)30494-4

DOI: https://doi.org/10.1016/j.apcata.2020.117901

Reference: APCATA 117901

To appear in: *Applied Catalysis A, General*

Received Date: 17 August 2020

Revised Date: 22 October 2020

Accepted Date: 24 October 2020

Please cite this article as: Mihai M-Alexandru, Culita DC, Atkinson I, Papa F, Popescu I, Marcu I-Cezar, Unraveling mechanistic aspects of the total oxidation of methane over Mn, Ni and Cu spinel cobaltites via *in situ* electrical conductivity measurements, *Applied Catalysis A, General* (2020), doi: https://doi.org/10.1016/j.apcata.2020.117901

Unraveling mechanistic aspects of the total oxidation of methane over Mn, Ni and Cu spinel cobaltites via *in situ* electrical conductivity measurements

Marius-Alexandru Mihai[1,2], Daniela Cristina Culita[2], Irina Atkinson[2], Florica Papa[2], Ionel Popescu[3], Ioan-Cezar Marcu[1,3,*]

[1] Laboratory of Chemical Technology and Catalysis, Department of Organic Chemistry, Biochemistry and Catalysis, Faculty of Chemistry, University of Bucharest, 4-12, Blv. Regina Elisabeta, 030018, Bucharest, Romania.

[2] "Ilie Murgulescu" Institute of Physical Chemistry of the Romanian Academy, 202, Spl. Independentei, 060021, Bucharest, Romania.

[3] Research Center for Catalysts and Catalytic Processes, Faculty of Chemistry, University of Bucharest, 4-12, Blv. Regina Elisabeta, 030018, Bucharest, Romania

[*] Corresponding author: E-mail address: ioancezar.marcu@chimie.unibuc.ro (I.-C. Marcu).

Graphical abstract

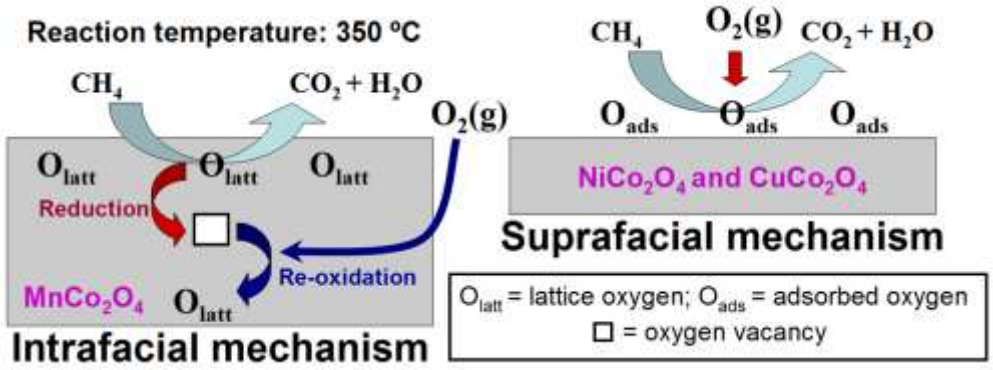

Research highlights

- Mn and Cu cobaltites behave as semiconductors of n-type and p-type, respectively.
- Ni cobaltite is in a metallic conductivity state.
- $NiCo_2O_4$ and $CuCo_2O_4$ are not reduced under the reaction mixture: suprafacial mechanism.
- $MnCo_2O_4$ is reduced in the reaction conditions: heterogeneous redox mechanism.
- $CuCo_2O_4$ has the highest density of charge carriers and is the most active catalyst.

ABSTRACT

Mn, Ni and Cu cobaltite spinels were synthesized by coprecipitation, characterized and evaluated in the total oxidation of methane. To gain a deeper insight into their catalytic behavior, their electrical conductivity was studied as a function of temperature and oxygen partial pressure, and was followed with time during sequential exposures to different gases in conditions close to those used for the catalytic tests. The Ni cobaltite is in a metallic conductivity state and cannot be reduced in the reaction conditions, suggesting that it functions via a suprafacial mechanism. The Cu cobaltite behaves as a p-type semiconductor, but it is not reduced under the reaction mixture at the reaction temperature of 350 °C,

suggesting that, at least in these conditions, the suprafacial mechanism is operating. The Mn cobaltite has an n-type semiconducting character and is reduced in the reaction conditions, suggesting that a heterogeneous redox mechanism is involved.

KEYWORDS: spinel; cobaltite; electrical conductivity; total oxidation; methane; reaction mechanism

1. Introduction

Atmospheric pollutants are one of the most serious life threats on our planet. They are mostly generated in industrial processes and transportation [1]. Some examples are the volatile organic compounds (VOC) like formaldehyde [2-4] or methane [5-9], inorganic compounds like nitrogen oxides [10-12] or even solid microscopic carbon particles [13-15]. The way they harm life differs as ones are toxic and/or carcinogenic and others affect the global temperature having a greenhouse effect, measured by the Global Warming Potential (GWP) factor, e.g. methane has a GWP of 21, while N_2O has a GWP of 310 [7,11,12]. Therefore, it is necessary to convert the harmful compounds into less or even no dangerous compounds like CO_2, H_2O, N_2 etc. In the case of VOC, this can be done either by simply burning the exhaust gases which is energy costly, or by catalytic combustion. The latter is currently conducted on supported noble metal catalysts, but although they show high activity and selectivity toward total oxidation compounds [3,5-9,11,16,18], they still have some disadvantages like high sintering rates, volatility, poison-sensitive (especially to sulphur compounds and water), are inhibited by carbon monoxide and are also very expensive [19]. Nevertheless, they are currently used in the three-way catalysts (TWC) of petrol or natural gas internal combustion engines [5,7,9,11,17]. An alternative to noble metals is that of variable oxidation state metal oxides, especially transition-metal oxides, which can have outstanding catalytic properties in redox reactions [9,11,20]. They are strong competitors to noble metal-based catalysts not only because of their high abundance and low cost but also due to some other advantages like ease of preparation, higher resistance to sintering and greater chemical resistance (resistance to poisoning) [1,21,22]. Among them, the spinel-structured mixed oxides seem to show quite impressive catalytic performance in the total oxidation reactions [3,5,7,11,14-18,23,24], a book chapter being already dedicated to this subject [25]. A key particularity of spinel oxides is the inversion parameter, denoted with *i*, expressing the degree of inversion of a specific spinel-structured compound, accurately described by the general formula $[A_{1-i}^{p+}B_i^{q+}]_{T_d}[A_i^{p+}B_{(2-i)}^{q+}]_{O_h}O_4$, where usually *A* is a bivalent cation and *B* is a trivalent

cation, located in either tetrahedral (T_d) or octahedral (O_h) sites. This parameter can be manipulated by thermal or other treatments [26] and, because spinels preferably expose the octahedral sites, rather than the tetrahedral ones, as previously demonstrated by Low Energy Ion Scattering (LEIS) analysis [27,28], the surface population of active sites of a spinel-based catalyst can be controlled [28].

Methane total oxidation is a widely used reaction for testing the performance of different total oxidation catalysts. Research is intensively conducted on finding efficient catalysts based on transition metal oxides and mixed-metal oxides, including spinel-structured cobaltites which showed excellent performance. Indeed, from a series of cobalt-nickel mixed oxides with different Co/Ni ratios, the CoNi (50:50) catalyst was shown to be the most active for methane combustion, its performance being close to that of Pd/γ-Al_2O_3 [6]. This performance was ascribed to the formation of a distorted $NiCo_2O_4$ spinel structure which was shown to enhance the adsorption of oxygen [6]. In a series of mesoporous MCo_2O_4 (M = Cu, Zn and Ni) spinels, $CuCo_2O_4$ was shown to be the most active catalyst in methane combustion, its superior activity being attributed to a high normalized amount of Co^{3+} cations on the surface [29]. Among co-precipitated MCo_2O_4 (M = Ni, Co, Mn, Fe, Cu) spinels, $NiCo_2O_4$ emerged as the best catalyst for the complete oxidation of a CO-CH_4 mixture, with a total conversion temperature (T_{100}) of only 350 °C [7]. This was 70 °C lower than that observed for the complete oxidation of pure methane, obviously due to a synergistic effect between CO and CH_4 [5]. This effect was also reported in the total oxidation of a CO-LPG (liquefied petroleum gas) mixture over spinel-structured MCo_2O_4 (M = Ni, Cu, Zn) catalysts [17]. With $NiCo_2O_4$, the most active catalyst in this series, total conversion was achieved at 185 °C for CO-LPG mixture and at 195 °C for LPG alone [17]. In the total oxidation of propane and CO over spinel-structured Co-Mn mixed oxides with different cation ratios, $Co_xMn_{3-x}O_4$ ($0 \leq x \leq 3$), the optimum system with x = 2.3 was significantly more active than the best Co_3O_4 catalysts reported in the literature [16]. Modifying Co_3O_4 spinel with 2 wt. % ZrO_2 resulted in an enhanced activity in the total oxidation of methane corresponding to 90 % conversion at a temperature as low as 377 °C due to increased concentrations of surface Co^{2+} and adsorbed oxygen species [30]. Spinel oxides, such as Co_3O_4 [3] and $Ni_{0.8}Co_{2.2}O_4$ [18], were shown to be, with $T_{100} \approx 90$ °C, among the most active catalysts for the complete oxidation of formaldehyde. All these results clearly point out the versatility and high performance of total oxidation catalysts based on cobaltite spinels and justify a study focused on the deep understanding of their functioning mechanism.

In the present work, the mechanism involved in the complete oxidation of methane over three spinel-structured metal cobaltites, i.e. $MnCo_2O_4$, $NiCo_2O_4$ and $CuCo_2O_4$, is studied by means of *in situ* electrical conductivity measurements, a powerful technique that can reveal the phenomena standing

behind an oxidation catalytic process conducted on semiconductor oxide catalysts [31]. This method was successfully applied to study several total or partial oxidation reactions over different oxide-based catalysts, such as the total oxidation of methane over perovskite [32,33] and $CuFe_{2-x}Mn_xO_4$ spinel [34] catalysts, the complete oxidation of different VOC [35] or the CO, ethene and soot combustion [36] over Cu-Ce oxides, the total oxidation of methane and the preferential oxidation of CO over Ce-Pr oxides [37], isobutane oxydehydrogenation over phosphated ceria [38], n-butane oxydehydrogenation over metal pyrophosphates [39], propane ammoxidation over V and Fe antimonates [40] or VAlO mixed oxides [41], and n-butane oxidation to maleic anhydride over V-P-O catalysts [42].

2. Experimental

2.1. Catalysts synthesis

All compounds were used as received from the supplier without any further processing: $Co(NO_3)_2 \cdot 6H_2O$ (Sigma-Aldrich), $Mn(NO_3)_2 \cdot 4H_2O$ (Carl Roth), $Ni(NO_3)_2 \cdot 6H_2O$ (Merck), $Cu(NO_3)_2 \cdot 3H_2O$ (Sigma-Aldrich) and Na_2CO_3 (Sigma-Aldrich). The three cobaltites, $MnCo_2O_4$, $NiCo_2O_4$ and $CuCo_2O_4$, were synthesized by a coprecipitation method. This consisted in the slowly dropwise addition of a 3 M metal nitrates (M/Co mol ratio of 1/2, M = Mn, Ni or Cu) solution to the equivalent volume of a 1.5 M solution of Na_2CO_3, at room temperature, under vigorous stirring and careful pH value monitoring. In the solution of metal nitrates, the Co and metal M contents corresponded to 5 g of MCo_2O_4. The target pH was set to 9.0, the starting value being of ca. 12, which corresponds to the 1.5 M Na_2CO_3 solution. To maintain the pH value to 9.0, excess portions of 1.5 M Na_2CO_3 were dropwise added to the reaction mixture along with the solution of metal nitrates. The slurry was further mixed for 30 minutes, and then vacuum filtered and thoroughly washed with double distilled water. Afterwards the washed precipitate was dried for 22 h at 120 ºC and finally calcined at 450 ºC for 5 h in static air.

It is worth noting that the synthesis method was chosen to obtain improved textural and catalytic properties of the cobaltites. Indeed, sodium carbonate was shown to generate catalytic materials with enhanced total oxidation activity compared to other precipitating agents [5-7,10,17]. Moreover, due to its porogenic effect, increased specific surface areas of the calcined catalysts are expected [3,5]. Although both the addition of the precipitating agent to the mixed-metal solution [3,6,10] and the addition of the mixed-metal solution to the precipitating agent [5,7,17] were applied to obtain metal cobaltites, we carried out the coprecipitation by adding the mixed-metal solution to the precipitating agent in order to avoid the formation of an inhomogeneous coprecipitate [43].

2.2. Catalyst characterization

The powder X-Ray diffraction (XRD) analysis was conducted on a Rigaku Ultima IV diffractometer using a monochromatic Cu K_α (λ = 1.5418 Å) radiation source operated at 40 kV and 30 mA. The diffractograms were registered on a 5 - 85° 2θ range with a 2° min^{-1} scan speed and a 0.02° step width. XRD data were analyzed using Rigaku's PDXL software connected to ICDD PDF-2 database. Quantitative X-ray powder diffraction analysis was performed using the Reference Intensity Ratio (RIR) method. The average crystallite size was calculated using the Williamson-Hall method.

Porosity and surface area of the samples were determined by nitrogen adsorption-desorption analysis at -196 °C using a Micromeritics ASAP 2020 analyzer. The samples were outgassed at 300 °C for 3 h before analysis. Specific surface areas (S_{BET}) were calculated using the Brunauer-Emmett-Teller (BET) equation. The total pore volume (V_{total}) was estimated from the amount adsorbed at the relative pressure of 0.99. The average pore diameter and pore size distribution curves were obtained from the desorption branch of the isotherm using Barrett–Joyner–Halenda (BJH) method.

Scanning electron micrographs (SEM) and energy-dispersive X-ray (SEM) measurements were acquired using a field emission gun scanning electron microscope (FEG-SEM) Nova NanoSEM 630 equipped with an EDX module (FEI Company, USA), working at a high voltage of 20 kV. Four different small areas were analyzed on each sample, as shown in Fig. S1.

Temperature-programmed reduction under hydrogen (H_2-TPR) and temperature-programmed oxidation under oxygen (O_2-TPO) measurements were performed on a Chembet 3000-Quantachrome analyzer connected to a thermal conductivity detector (TCD) through a silica gel trap. The catalyst samples (ca. 30 mg) were heated up to 150 °C in an inert argon gas flow, cooled down to room temperature and then subjected to 5 % H_2 in Ar reducing gas mixture, with a 70 mL min^{-1} flow rate and a 10 °C min^{-1} heating rate until 820 °C. After cooling down to room temperature, the reduced samples were reoxidized by a gas mixture of 5 % O_2 in He, using the same temperature program as for the H_2-TPR.

2.3. Catalytic tests

The catalytic tests were conducted in an 18 mm diameter quartz tube fixed-bed down-flow reactor, operating at atmospheric pressure, loaded with 1 cm^3 of finely powdered catalyst supported on quartz

wool with the dead volumes filled with quartz chips. The reaction temperature was controlled by an electric furnace surrounding the reactor and the axial temperature profile (reported catalytic reaction temperature) was measured using an electronic thermometer placed in a thermowell centered in the catalyst bed. The volume hourly space velocity (VHSV) was set to 20,000 h^{-1} which for 1 cm^3 of catalyst corresponds to a 333.3 mL min^{-1} gas flow rate consisting of 1 vol. % methane in air. The gas flow rates were controlled by fine needle valves and measured with capillary flow meters. The catalyst masses corresponding to 1 cm^3 bed volume were 0.31, 1.17 and 0.71 g for Mn, Ni and Cu cobaltite, respectively.

Before the catalytic tests, the catalyst was pre-treated for ca. 20 min in a stream of air at 440 °C (heating rate of 10 °C min^{-1}), in order to clean its surface and to improve the test reproducibility. Activity measurements were performed by decreasing the reaction temperature from 440 °C at regular intervals of 20 °C until a conversion of ca. 10 % was achieved, and then the interval was reduced to 10 °C in order to obtain accurate data for kinetic analysis. The system was allowed to stabilize to the desired temperature for at least 15 min before the first product analysis was done. Subsequent analyses were performed until two consecutive measurements were identical. The analyses were done online by a Clarus 500 gas chromatograph equipped with a thermal conductivity detector (TCD), using two packed columns in series (6 ft Hayesep and 10 ft molecular sieve 5 Å). The conversion of methane was calculated based on product analysis in steady state conditions. Complete selectivity to CO_2 and H_2O was always observed.

2.4. Electrical conductivity measurements

To ensure good electrical contacts between the catalyst grains, the powders were compressed into pellets prior to the electrical conductivity measurements. The pellets were obtained by mixing the spinel powder (ca. 1.2 g) with a few drops of 5 % aqueous solution of poly(vinyl alcohol) (PVA) in order to ensure the necessary lubrication and adhesion between grains, this mixture being then pressed using a Carver 4350.L pellet press at a pressure of ca. 2.76×10^7 N m^{-2} (4000 psi). Finally, the pellets were calcined in static air at 450 °C for 5 h, in order to eliminate the PVA residue [44]. The obtained pellet was placed between two platinum electrodes in a horizontal quartz tube surrounded by an electrical furnace. The temperature was controlled using Pt-Rh thermocouples soldered to the electrodes. Flow rates of gases flowing over the pelletized sample were controlled by fine needle valves and were measured by capillary flow meters. The platinum electrodes were used for the measurement of the electrical resistance of the pellet with a FLUKE 177 multimeter set to ohmmeter. The electrical resistance value was converted into electrical conductivity (σ) by using the following equation:

$$\sigma = \frac{1}{\rho} = \frac{1}{R} \cdot \frac{h}{S} \quad (1)$$

where ρ is the electrical resistivity of the material, R is the measured electrical resistance, h is the thickness of the sample (ca. 0.3 cm) and S is the cross-section area of the platinum electrodes of the cell (whose diameter is 1.3 cm), i.e. the contact area between the metallic conductor and the semiconductor sample. The electrical conductivity of a pelletized powder sample is a function of the concentration of the charge carriers and it is given by the formula [31]:

$$\sigma = Ac \quad (2)$$

where c is the concentration of the main charge carriers and A is a constant that includes the charge of the electron, the mobility of the charge carriers and the number and quality of the contacts between the grains. Although the samples do not have similar surface areas (Table 1), since they were compressed at the same pressure and the electrical conductivity measurements were standardized, A can be considered similar for all the samples under identical conditions. In all the experiments, in order to eliminate any adsorbed impurities, the samples were first heated in air to the maximum temperature of 450 °C, cooled down to 200 °C and then heated again to the desired temperature with a rate of 5 °C min^{-1}. In these conditions, the concentration of adsorbed ionic species like HO^- or H_3O^+ that are able to induce additional surface conductivity is negligible.

3. Results and discussion

3.1. Catalyst characterization

The powder XRD patterns (Fig. 1) confirm the presence of the spinel phase in all cobaltites. Pure spinel phase was observed only in the case of Mn cobaltite (PDF # 00-023-1237), while Ni cobaltite (PDF # 01-073-1702) and Cu cobaltite (PDF # 00-001-1155) also contain certain amounts of NiO (PDF # 00-047-1049) and CuO (PDF # 00-048-1548) side phases, respectively (Table 1). The phase separation in the case of Ni cobaltite is likely due to the harsh calcination conditions used, i.e. 450 °C for 5 h, in line with the reported instability of the $NiCo_2O_4$ spinel above 400 °C [6,10,29]. However, it is noteworthy that pure $NiCo_2O_4$ spinel phases were reported for calcination temperatures as high as 500 °C [17] or 600 °C [5]. In the case of Cu cobaltite sample, the presence of CuO side phase is primarily caused by the thermal stability of copper-rich malachite phase that occurs in copper-containing hydroxycarbonate precursors, inducing phase segregation. This is known as the "impossibility of stoichiometric copper cobaltite being

synthesized from hydroxycarbonate precursors", as reported by Klissurski and Uzunova [45] and confirmed by Abu-Zied et al. [9]. Another reason for the presence of CuO side phase is the instability of $CuCo_2O_4$ at temperatures higher than 350 °C [45].

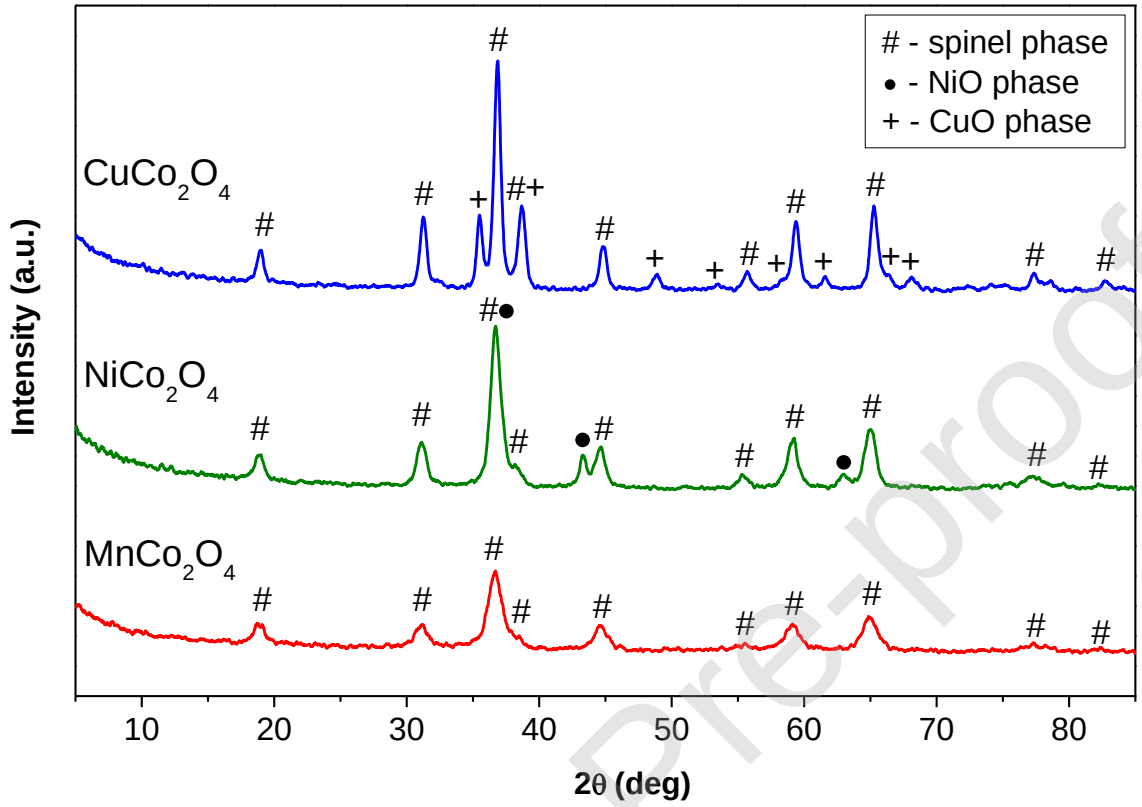

Figure 1. Powder XRD patterns of the prepared cobaltites.

The specific surface area, pore volume, pore size and crystallite size of the MCo_2O_4 spinels are listed in Table 1 and their corresponding adsorption-desorption isotherms and pore size distributions are shown in Figs. 2 and S2, respectively. All the samples reveal type IV isotherms according to the IUPAC classification, with H3-type hysteresis loop for $CuCo_2O_4$ spinel and a combination of H3 with H2b types hysteresis loops for $MnCo_2O_4$ and $NiCo_2O_4$ spinels, characteristic of mesoporous materials with slit-shaped pores and more complex pore structures, respectively [46]. The BET surface area (S_{BET}) decreases from 121 $m^2\ g^{-1}$ for $MnCo_2O_4$ to 30 $m^2\ g^{-1}$ for $CuCo_2O_4$, in agreement with the observed increase of the crystallite size of the materials (Table 1). Their pore size distributions (Fig. S2) obtained from the desorption branch of the isotherms indicate unimodal pore structures with well-defined maxima. The average pore size increases from 9.6 nm for $MnCo_2O_4$ to 35.7 nm for $CuCo_2O_4$, being inversely corelated with the evolution of the surface area of these materials. Their pore volume ranges between 0.27 $cm^3\ g^{-1}$ for $NiCo_2O_4$ and 0.37 $cm^3\ g^{-1}$ for $MnCo_2O_4$ (Table 1), irrespective of their surface area and pore size.

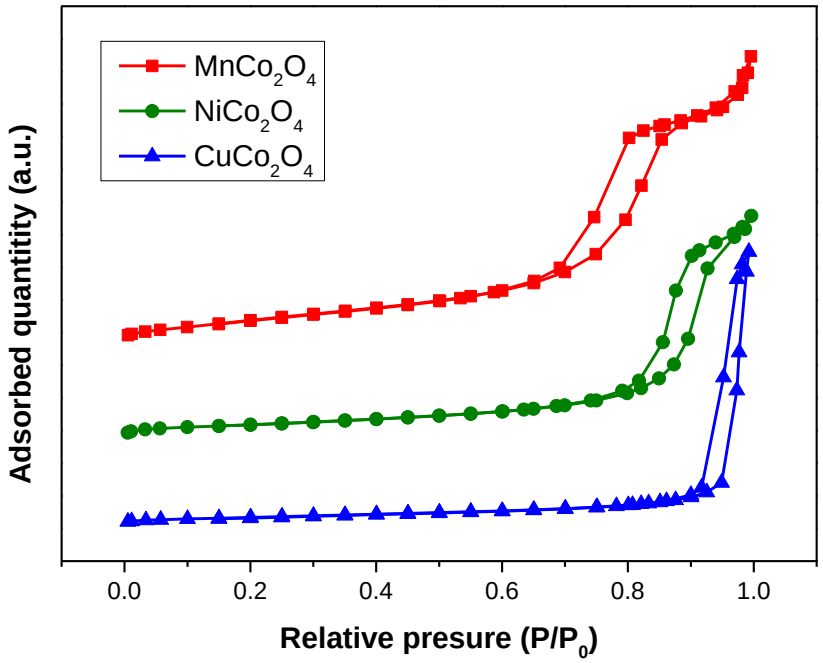

Figure 2. Adsorption isotherms for the synthesized cobaltites.

Table 1. Physicochemical characteristics of the prepared spinels.

Sample	*M/Co mol ratio*[a]	*Phase composition (%)*	*S_{BET} ($m^2 \cdot g^{-1}$)*	*Pore volume ($cm^3 \cdot g^{-1}$)*	*Pore size*[a] *(nm)*	*Crystallite size*[b] *(nm)*
$MnCo_2O_4$	0.43	$MnCo_2O_4$ (100)	121	0.37	9.6	7.6
$NiCo_2O_4$	0.52	$NiCo_2O_4$ (95.2) NiO (4.8)	55	0.27	15.3	8.7
$CuCo_2O_4$	0.53	$CuCo_2O_4$ (77.0) CuO (23.0)	30	0.33	35.7	15.1

[a] From EDX analysis (M = Mn, Ni and Cu, respectively). [b] Average pore size. [c] Calculated for the spinel phase from powder X-Ray diffraction data using the Scherrer equation.

The SEM images of the spinel cobaltites are shown on Fig. 3. It can be observed that Mn cobaltite is a fluffy aggregate of small particles, while Ni and Cu cobaltites are agglomerates of intermediate and large spherical particles, respectively. This is in line with the evolution of their surface area and Scherrer crystallite size. The compositions of the cobaltite samples were estimated by EDX analysis, the M/Co mol ratios (M = Mn, Ni and Cu) presented in Table 1 being in good agreement with the theoretical value. The lower Mn/Co molar ratio suggests a slight excess of Co in the Mn cobaltite whose chemical formula can be written $Mn_{1-x}Co_{2+x}O_4$. Although the M/Co molar ratios for Ni and Cu cobaltite samples are slightly higher than the stoichiometric 0.5 value, due to NiO and CuO phase separation, respectively, the spinel phase in these materials also contains an excess of Co and, hence, correspond to the chemical formula $M_{1-x}Co_{2+x}O_4$ (M = Ni and Co).

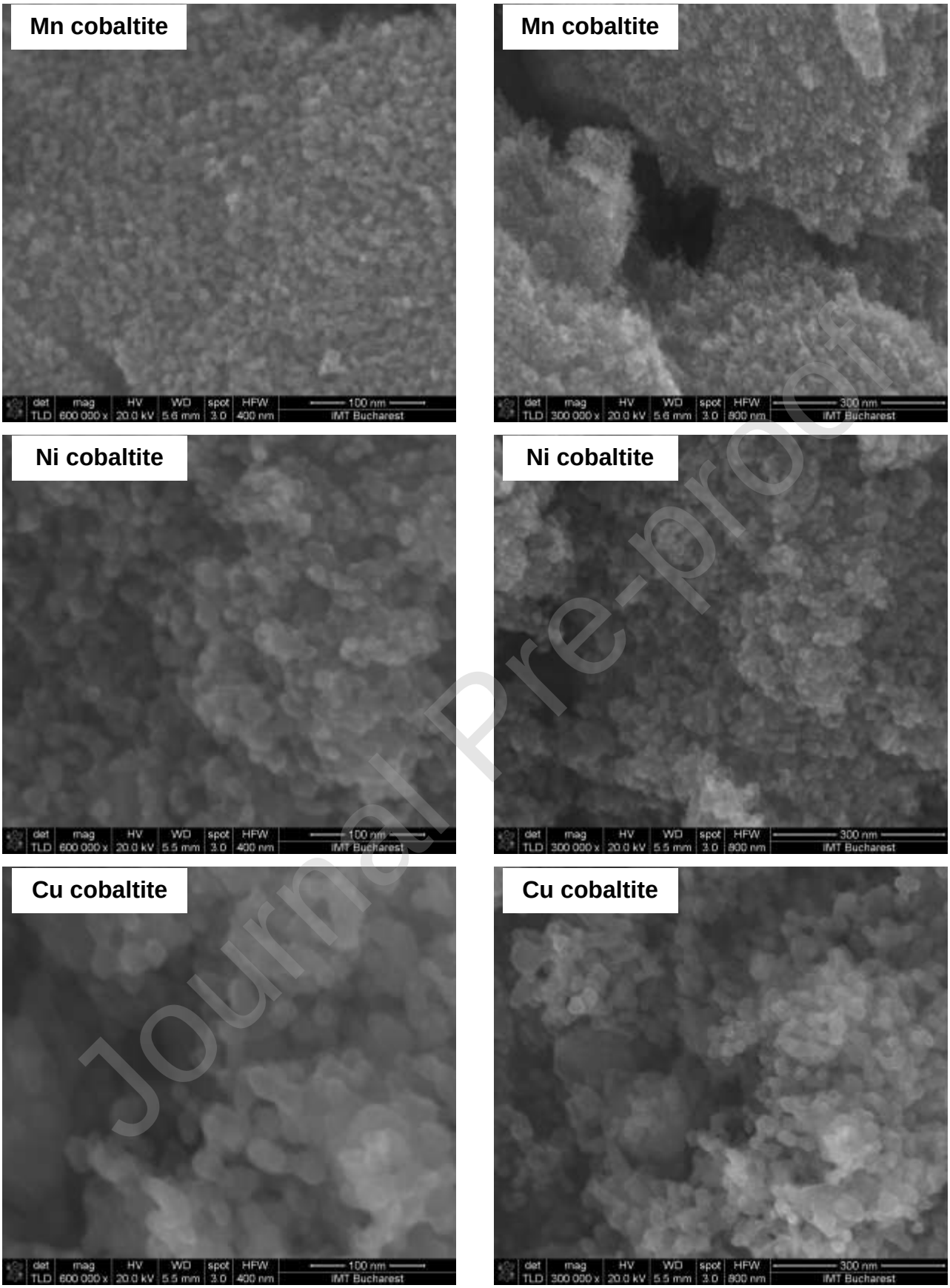

Figure 3. SEM images at two different magnifications of Mn, Ni and Cu cobaltite samples.

The reducibility of the spinel-structured cobaltites, investigated by H_2-TPR, is represented in Fig. 4. The $CuCo_2O_4$ composite spinel oxide shows a large reduction profile with several maxima corresponding to the reduction of copper and cobalt species. Thus, the two low-temperature maxima can be assigned to the reduction of Cu^{2+} to Cu^{+} and Cu^{+} to Cu^{0} from surface highly dispersed copper species, while the high-temperature maxima can be attributed to the stepwise reduction of Co^{3+} to Co^{2+} and Co^{2+} to Co^{0}, together with the Cu^{2+} to Cu^{0} in bulk-phase co-reduction [47, 48]. The reduction process ends at 457 °C. In the case of $NiCo_2O_4$ spinel, two obvious reduction events can be observed in the low and high temperature regions. The low-temperature hydrogen consumption event with the maximum located at 323 °C can be assigned to the reduction of Co^{3+} to Co^{2+}. The high-temperature reduction signal is broad and correspond to two superimposed processes, i.e. the reduction of Ni^{2+} to Ni^{0} from both separated NiO and spinel $NiCo_2O_4$ phases, and the reduction of Co^{2+} to Co^{0} [5-7,49,50]. The reduction temperature range for Ni cobaltite extends to higher temperature, i.e. 520 °C, suggesting its lower reducibility compared to Cu cobaltite. Two reduction events, in the low and high temperature regions, can also be observed for $MnCo_2O_4$. The first reduction peak, with several maxima, extending from ca. 130 to 430 °C, corresponds to the successive reduction of Co^{3+} to Co^{2+}, Mn^{4+} to Mn^{3+}, and Co^{2+} to Co^{0}, while the broad peak with the maximum at 519 °C corresponds to the reduction of Mn^{3+} to Mn^{2+} [51, 52]. Among the three cobaltite spinels, Mn cobaltite is the last to finish the reduction process, with the high-temperature peak positioned at a temperature where both Cu and Ni cobaltites are already totally reduced. The data in Table 2 show that the latter were completely reduced, while the degree of reduction of Mn cobaltite is limited to 88.4 %, likely due to the limited capability of Mn cations to reach Mn^{0} oxidation state in the studied temperature interval. The tail observed in the TPR profile of $MnCo_2O_4$ after the last reducing peak (Fig. 4) indicates that the reduction process is not over, most likely due to the ability of the newly formed metallic Co particles to dissociate the hydrogen molecules and thus favoring the further reduction process of Mn^{2+} species. Indeed, this hydrogen spillover effect was reported for other Co-containing mixed oxides, such as Co_3O_4-CeO_2 systems [53] and Co-Mn-Al spinel oxides [54].

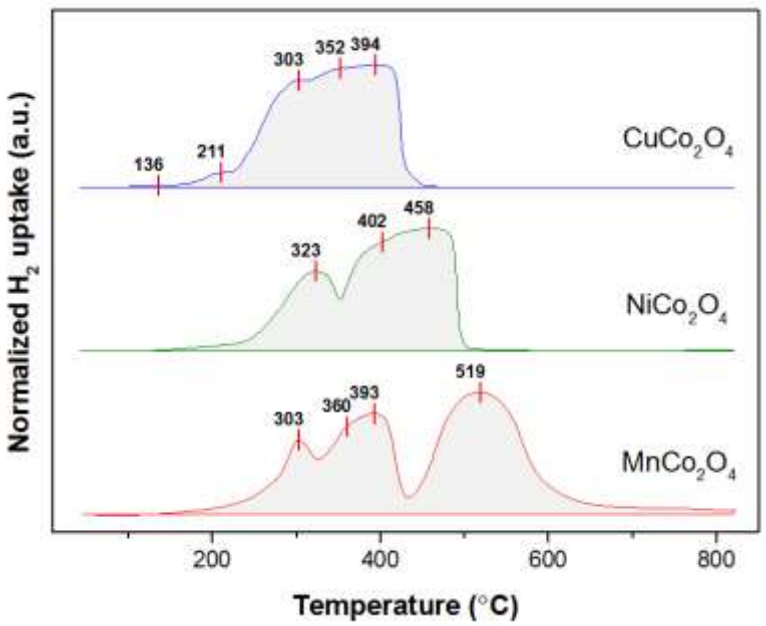

Figure 4. Normalized H_2-TPR curves of the cobaltites.

Table 2. Hydrogen consumptions of MCo_2O_4 spinels in H_2-TPR experiments and oxygen consumptions of the reduced spinels in O_2-TPO experiments.

Catalyst	*Maximum hydrogen consumption[a] (µmol/g)*	*Measured hydrogen consumption (µmol/g)*	*Degree of reduction (%)*	*Measured oxygen consumption (µmol/g)*	*Degree of reoxidation (%)*
$MnCo_2O_4$	16,893	14,933	88.4	6,333	84.8
$NiCo_2O_4$	16,628	16,637	100.1	7,431	89.4
$CuCo_2O_4$	16,299	16,643	102.1	7,839	96.2

[a] Calculated for the MCo_2O_4 stoichiometry and considering the reduction of all cations to their zero-valence state.

To check the capacity of reoxidation of the reduced spinel cobaltites, O_2-TPO runs were carried out after the H_2-TPR measurements, the TPO profiles obtained being shown in Fig. 5. Broad features, with several maxima, extending up to 650 °C for Mn cobaltite and to 800 °C for Cu and Ni cobaltites can be observed reflecting both the complex redox chemistry of the involved transition metals [55] and the existence of metallic particles of different sizes in the reduced material [56]. The low-temperature peaks at 226 and 248 °C for reduced Cu and Ni cobaltites, respectively, could be attributed to the reoxidation of copper and nickel metallic particles resulted from the reduction of CuO and NiO side phases, respectively, identified in the initial material. The successive peaks above 300 °C can be attributed to the oxidation of metallic species from the M-Co (M = Mn, Co and Ni) metallic alloy particles likely formed by the reduction of MCo_2O_4 spinel phase, to M^{2+} (with M = Mn, Co, Ni and Cu) and, then, to M^{3+} (with M = Mn

and Co) and M^{4+} (with M = Mn). The total oxygen consumptions calculated from the TPO profiles and the degrees of reoxidation calculated considering a degree of reduction of 100 % for Cu and Ni cobaltites and of 88.4 % for Mn cobaltite, are reported in Table 2. It can be observed that, although the degrees of reoxidation are very high, the reduced cobaltites were not totally reoxidized. This suggests that the bulk of the reoxidized particles contains transition metal species in lower valence state, likely including metallic zerovalent state. The reoxidation ability of the three samples in terms of oxygen consumption increases following the order $MnCo_2O_4$ < $NiCo_2O_4$ < $CuCo_2O_4$.

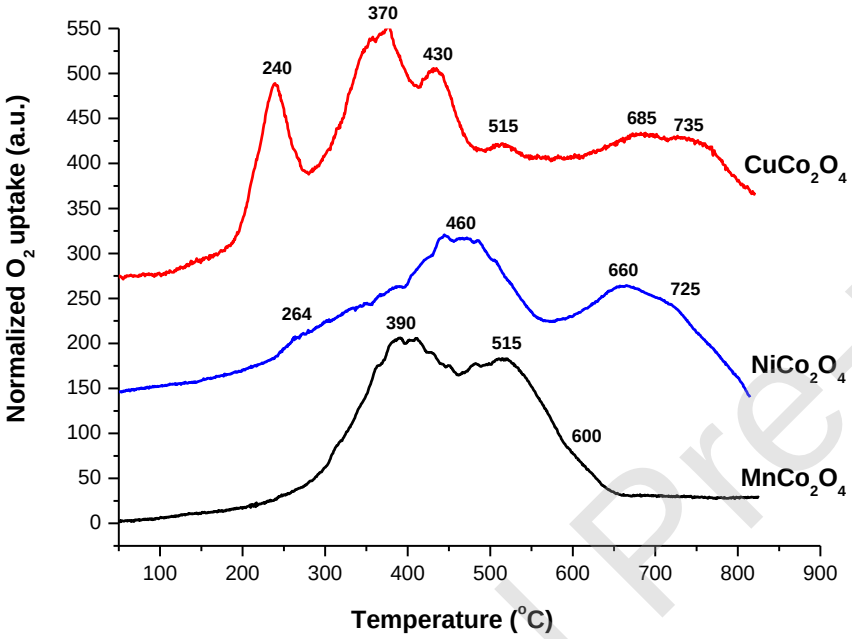

Figure 5. Normalized O_2-TPR curves of the reduced cobaltites.

The H_2-TPR together with subsequent O_2-TPO experiments evidenced high reduction and reoxidation abilities of the studied spinel cobaltites.

3.2. Catalytic properties

The conversion vs. temperature curves for the total oxidation of methane, as a model molecule, over the cobaltite catalysts, limited to a temperature lower than their calcination temperature, are depicted in Fig. 6. For comparison purposes, the curve of a reference Pd/Al_2O_3 catalyst tested in similar conditions and previously reported in Ref. [57] is also shown in Fig. 6. It can be observed that the best catalyst is the copper cobaltite, $CuCo_2O_4$, which, in the low conversion domain, is even better than the reference Pd/Al_2O_3 system. For conversion values higher than ca. 10-15 %, the methane conversion increases slowly

with reaction temperature for all the cobaltite catalysts indicating that the diffusional influences become significant. Within all the temperature range studied, the activity of the cobaltites follows the order: $CuCo_2O_4$ > $NiCo_2O_4$ > $MnCo_2O_4$. It is worth noting that the relative activity of similar catalytic materials in the total oxidation of different molecules reported in the open literature is quite different from that reported here for methane total oxidation. Thus, the order of activity of coprecipitated cobaltites calcined at 400 °C under a 4.5 vol. % CO in air gas mixture in the total oxidation of a 1.5 vol. % CO – 1.5 vol. % CH_4 in air mixture was: $NiCo_2O_4$ > $MnCo_2O_4$ > $CuCo_2O_4$ [7]. Also, for similarly prepared cobaltites, calcined at 300 °C, $NiCo_2O_4$ was shown to be more active than $CuCo_2O_4$ in the total oxidation of liquefied petroleum gas (2.5 vol. % LPG in air) [17]. On the other hand, for mesoporous spinel cobaltites prepared by the nanocasting method using mesoporous SBA-15 silica as a hard template and calcined in air at 380 °C, the activity in the oxidation of CO (1 vol. % CO in air) in the low conversion range followed the order: $MnCo_2O_4$ > $CuCo_2O_4$ > $NiCo_2O_4$, the latter also showing a continuous deactivation on stream [23]. These data show that the catalytic behavior of the cobaltite spinels is a complex function of different factors, such as the method of preparation, including the temperature and atmosphere of calcination, the nature of the molecule to be oxidized etc.

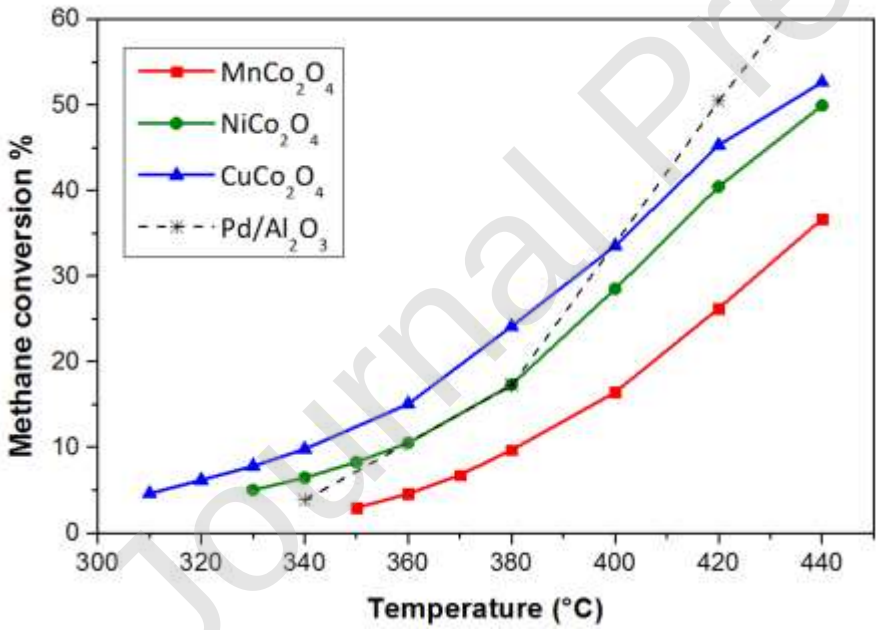

Figure 6. Conversion vs. temperature sigmoids for the synthesized materials and the Pd/Al_2O_3 reference in methane total oxidation.

The temperature corresponding to 10 % methane conversion (T_{10}), both the intrinsic and specific activities at 360 °C and the apparent activation energy, E_a, obtained from the Arrhenius plots shown in Fig. S3, are summarized in Table 3. It can be observed that not only in terms of conversion but also in

terms of reaction rate the copper cobaltite is the most active catalyst in this series. Notably, its intrinsic activity is more than four times higher than that of the nickel cobaltite, while the corresponding activation energy is only slightly lower. This suggests that the nature of the active site is not too different in the two catalytic materials, but the copper cobaltite contains a significantly higher density of active sites compared to the nickel cobaltite. On the other hand, the activation energy for the manganese cobaltite is significantly higher compared to the two other cobaltites, accounting for its lowest intrinsic activity and suggesting a quite different nature of the active site in this material. The higher specific activity observed for the manganese cobaltite compared to the nickel cobaltite is obviously due to the significantly higher surface area of the former.

Table 3. Catalytic properties of the cobaltite materials in methane combustion.

Catalyst	***T_{10} (°C)***	***Reaction rate at 360 °C***		***E_a ($kJ \cdot mol^{-1}$)***
		Specific (10^{-7} $mol \cdot s^{-1} \cdot g^{-1}$)	*Intrinsic (10^{-9} $mol \cdot s^{-1} \cdot m^{-2}$)*	
$MnCo_2O_4$	381	3.38	2.79	134.8
$NiCo_2O_4$	358	2.03	3.70	78.3
$CuCo_2O_4$	341	4.84	16.18	74.3

3.3. Electrical conductivity measurements

To gain a deep understanding of the catalytic behavior of the cobaltite materials in the complete oxidation of methane, their redox and semiconductive properties were studied by *in situ* electrical conductivity measurements as a function of temperature in the reaction temperature range, of oxygen partial pressure and of the nature of the gas phase in contact with the solid, including the reaction mixture, at constant temperature of 350 °C which is in the kinetic domain for all the catalysts.

3.3.1. Conductivity variations of the cobaltites as a function of temperature

The conductivities of the three cobaltite-based materials were studied under air at atmospheric pressure in the temperature interval between 200 and 450 °C. The variations of electrical conductivity as a function of temperature are displayed in Fig. 7a, while the variations of log(σ) as a function of the reciprocal absolute temperature (Arrhenius plots) are plotted in Fig. 7b. For both Cu and Mn cobaltites the electrical conductivity increases exponentially with temperature accounting for a typical semiconducting behavior, while for Ni cobaltite the electrical conductivity is high and does not vary with temperature accounting for a quasi-metallic conducting behavior. To explain this behavior, it is worth remembering that in spinels, including cobaltites, a $\sigma^*(e_g)$ band is formed by strong covalent B-O-B type

interaction between the octahedral B-site cations, as shown for Co_3O_4 and $Co_{3-x}Ni_xO_4$ systems [58,59]. When this band is empty, as in the case of Co_3O_4 spinel (octahedral B-site Co^{3+} cations have the electronic configuration $t_{2g}^6 e_g^0$), or when the charge carriers are present as in the case of $Co_{3-x}Ni_xO_4$ system for small values of *x* (octahedral B-site Ni^{3+} cations have the electronic configuration $t_{2g}^6 e_g^1$), but they are Anderson-localized, their density being lower than a threshold percolation concentration, the spinels have a semiconducting behavior [58,59]. An increased Ni^{3+} concentration in the octahedral B-sites of the spinel structure, which means an increased charge carriers concentration in the $\sigma^*(e_g)$ band, leads to the percolation of the conducting B-O-B chains throughout the lattice and, hence, to a metallic behavior, as observed for the $NiCo_2O_4$ spinel [58].

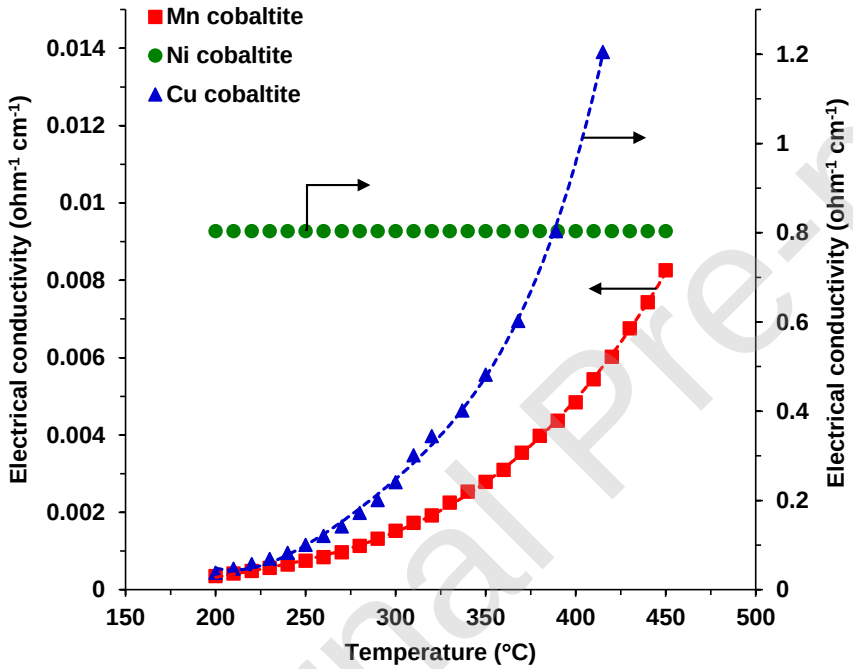

(a)

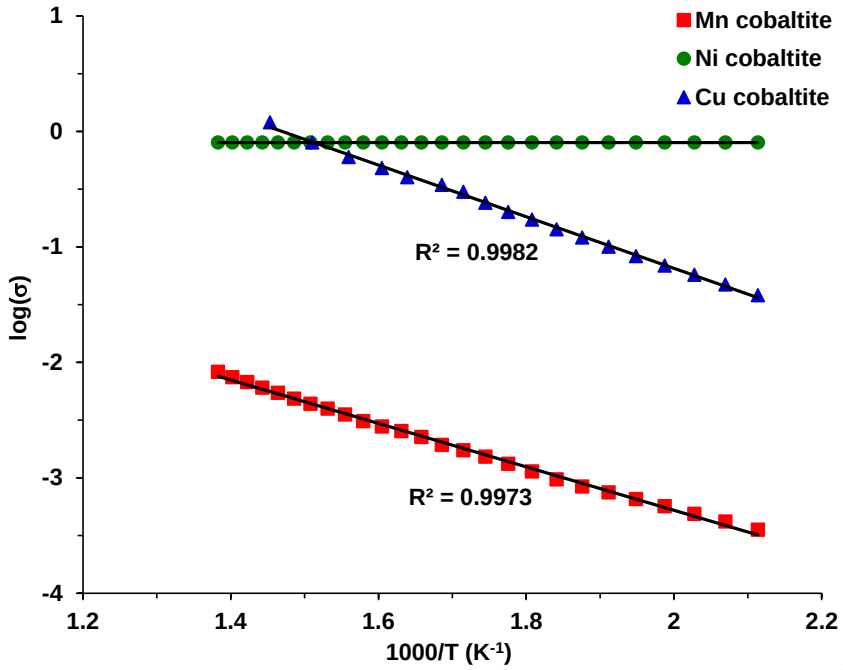

(b)

Figure 7. The electrical conductivity of the cobaltites as a function of the temperature (a) and variation of log(σ) as a function of the reciprocal absolute temperature (Arrhenius plots) (b).

The variation of the electrical conductivity (σ) of semiconductors with temperature is governed by the Arrhenius law:

$$\sigma = \sigma_0 e^{\left(-E_c/RT\right)} \tag{3}$$

where σ_0 is the pre-exponential factor, R is the universal gas constant, T is the absolute temperature and E_c is the activation energy of conduction. The logarithmation of Eq. (3) yields the following linear equation:

$$\ln \sigma = \ln \sigma_0 - \frac{E_c}{R} \cdot \frac{1}{T} \tag{4}$$

which describes the variations depicted in Fig. 5b and allows determining the σ_0 and E_c values for the cobaltites (Table 4). The σ_0 value, which is a material constant depending on the charge carrier concentration, is three orders of magnitude greater for $CuCo_2O_4$ than for the two other cobaltites. The E_c values are lower than 0.5 eV and fall within the range observed for similar materials at temperatures lower than ca. 400-450 °C [60-62]. The E_c value for $NiCo_2O_4$ is zero, in line with its quasi-metallic conductivity [59].

Table 4. Pellet densities and Arrhenius parameters for the electrical conductivity of the cobaltite spinels.

Sample	*Pellet density ($cm^3\ g^{-1}$)*	*E_c (eV)*	*σ_0 ($\Omega^{-1}cm^{-1}$)*
$MnCo_2O_4$	2.65	0.38	3.03
$NiCo_2O_4$	3.39	0.0	0.80
$CuCo_2O_4$	3.68	0.45	1.93×10^3

3.3.2. Conductivity variations of the cobaltites as a function of oxygen partial pressure

The electrical conductivity of the extrinsic oxide semiconductors is a function of the oxygen partial pressure, its variation at constant temperature being dependent on the type of the semiconductor, i.e. the electrical conductivity either increases with the oxygen partial pressure for p-type semiconductors or decreases for n-type semiconductors. This behavior is determined by the type of lattice defects in the material [31]. Therefore, electrical conductivity measurements as a function of oxygen partial pressure gives information about the type of semiconductor and the nature of point defects in the solid.

Fig. 8 displays the variation of the electrical conductivity with the oxygen partial pressure, P_{O_2}, at constant temperature of 350 °C which is in the kinetic domain for all the cobaltite-based catalysts. It can be observed that for both Ni and Cu cobaltites the electrical conductivity does not vary with the oxygen partial pressure. While for the Ni cobaltite, which is in a quasi-metallic conductivity state, this is rather expected [33], for the Cu cobaltite, this behavior suggesting an intrinsic conduction mechanism [31] is quite unexpected. Indeed, the latter is known to be a p-type semiconductor involving a small polaron hopping mechanism between the mixed valence cations located in the octahedral sites, as generally observed in spinel oxides, including cobaltites [63,64].

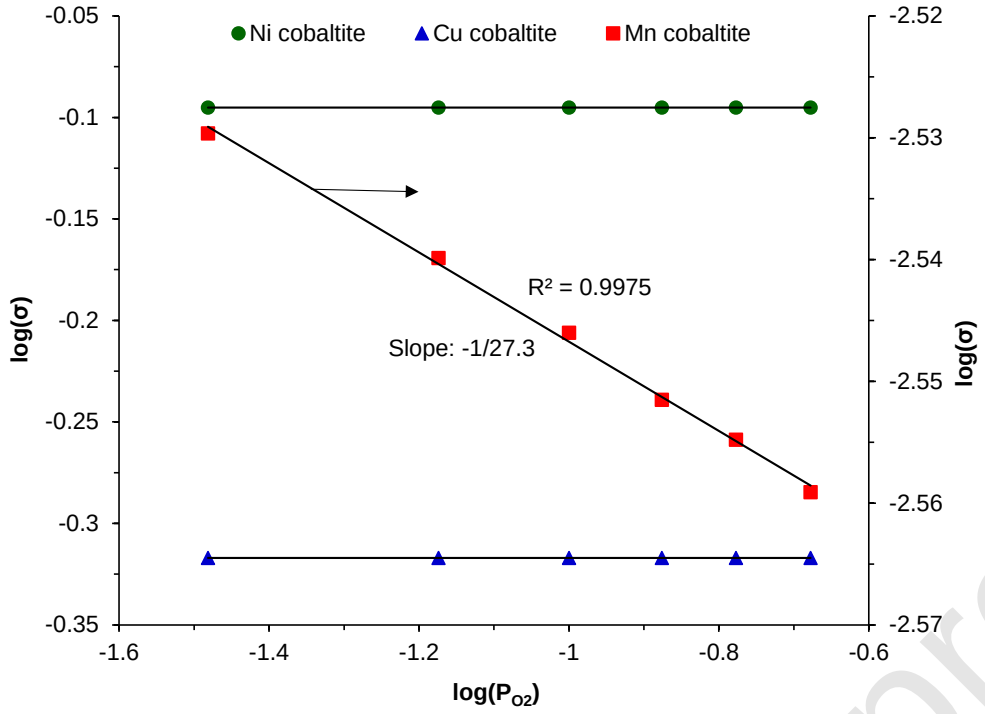

Figure 8. The log-log plot of the electrical conductivity (in ohm^{-1} cm^{-1}) of the cobaltite spinels as a function of the oxygen partial pressure (in atm) at 350 °C.

For the Mn cobaltite the electrical conductivity decreases with increasing the oxygen partial pressure, i.e. $\partial\sigma/\partial P_{O_2} < 0$, accounting for its extrinsic n-type semiconductivity [31]. Most likely, this is associated to the existence of anionic vacancies point defects in Mn cobaltite, which form according to the following equilibria written using the Kröger-Vink notation [65]:

$$O_O^{\times} \overset{K_1}{\leftrightarrow} \frac{1}{2}O_{2(g)} + V_O^{\bullet} + e' \qquad (5)$$

$$O_O^{\times} \overset{K_2}{\leftrightarrow} \frac{1}{2}O_{2(g)} + V_O^{\bullet\bullet} + 2e' \qquad (6)$$

where $O_O^{\times}$ represents an oxygen anion in regular lattice points, $V_O^{\bullet}$ and $V_O^{\bullet\bullet}$ represent singly and doubly ionized oxygen vacancies, respectively, and e' represents a quasi-free electron responsible for the n-type conductivity of the solid. Depending on which of equilibria (5) or (6) is dominant, the electrical conductivity will be a function of $P_{O_2}^{-1/4}$ or $P_{O_2}^{-1/6}$, respectively, and, hence, the slope of the $\log\sigma - \log P_{O_2}$ plot will be -1/4 or -1/6, respectively. The slope of the $\log\sigma - \log P_{O_2}$ plot for $MnCo_2O_4$ shown in Fig. 8 was found to be equal to -1/27, which is quite different from -1/4 or -1/6, suggesting that this spinel exhibit both electronic (σ_e) and ionic (σ_i) conduction, the total conductivity being:

$$\sigma = \sigma_e + \sigma_i \quad (7)$$

The electronic conductivity is expected to be a function of $P_{O_2}^{-1/4}$ or $P_{O_2}^{-1/6}$ depending on which singly or doubly ionized oxygen vacancies are dominant in the solid, while the ionic conductivity is independent of the oxygen partial pressure. To identify the most probable dependency of σ_e on the oxygen partial pressure and to confirm the conduction model proposed in Eq. (7) for the Mn cobaltite, the total conductivity σ was plotted as a function of both $P_{O_2}^{-1/4}$ and $P_{O_2}^{-1/6}$ (Fig. 9a), linear relationships being observed in both cases. However, the correlation coefficient being greater for the $P_{O_2}^{-1/6}$ than for the $P_{O_2}^{-1/4}$ dependency, the doubly ionized oxygen vacancies are considered to be dominant point defects in $MnCo_2O_4$. Therefore, the σ_i conductivity value for this sample at the temperature concerned, *i.e.* 350 °C, was calculated from the *y*-intercept of the plot in Fig. 9a and is equal to 2.23×10^{-3} $\Omega^{-1}cm^{-1}$. Then, the σ_e values corresponding to the different oxygen partial pressures were calculated by subtracting σ_i from σ according to Eq. (7), and were represented as a function of the oxygen pressure in a log–log plot (Fig. 9b). The obtained linear plot has a good correlation coefficient and exhibits the expected -1/6 slope confirming that the doubly ionized oxygen vacancies are the dominant point defects in the n-type Mn cobaltite. Notably, the lattice oxygen-anion conductivity (σ_i) is higher than the electronic conductivity (σ_e) within all the oxygen partial pressure range studied (Table S1).

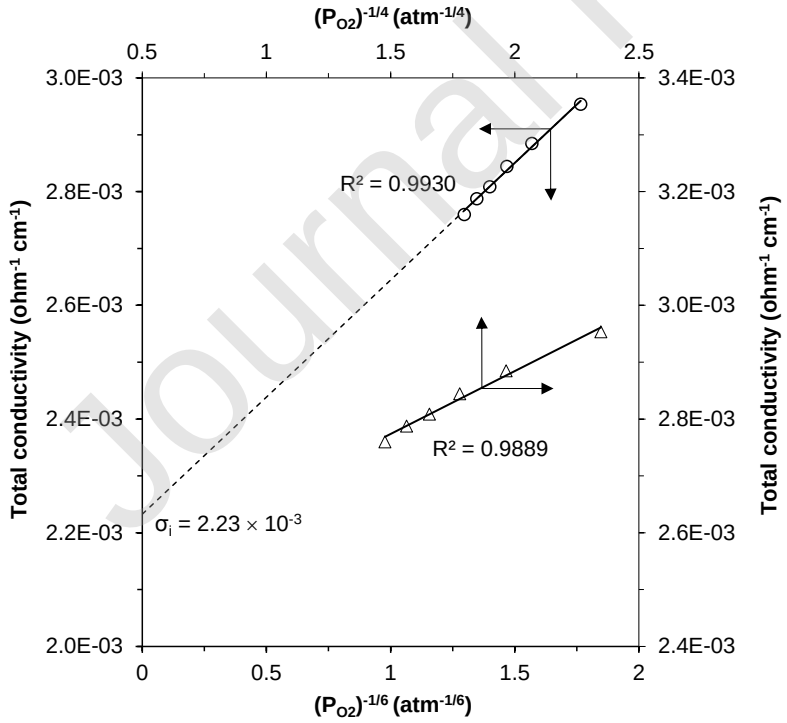

(a)

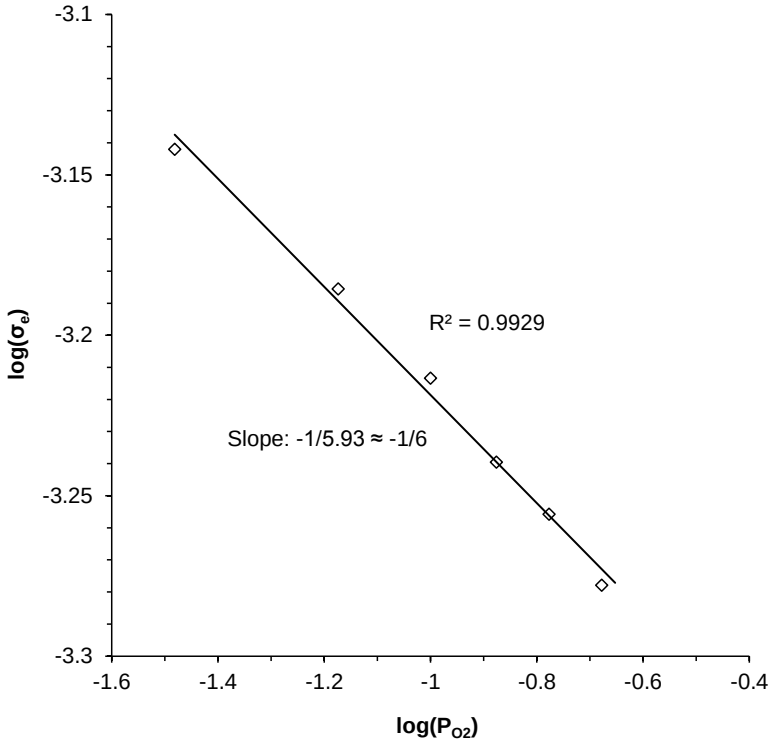

(b)

Figure 9. Total conductivity σ as a function of $(P_{O_2})^{-1/n}$ with n = 4 and 6, respectively (a), and electronic conductivity σ_e as a function of the oxygen partial pressure in a log-log plot (b) for the Mn cobaltite spinel.

3.3.3. Study of the redox behavior of the cobaltites by *in situ* electrical conductivity measurements

The redox behavior of the spinel cobaltites was studied by electrical conductivity measurement under different gases flowing over their surface, including the reaction mixture, i.e. 1 vol. % CH_4 in air, at constant temperature of 350 °C. The oxides were heated from room temperature to 350 °C, at a heating rate of 5 °C min^{-1} in an air flow at atmospheric pressure, and then they were maintained under air until reaching the steady state in these conditions before introducing successive sequences of different gas mixtures. The variations of the electrical conductivity observed are presented in Fig. 10.

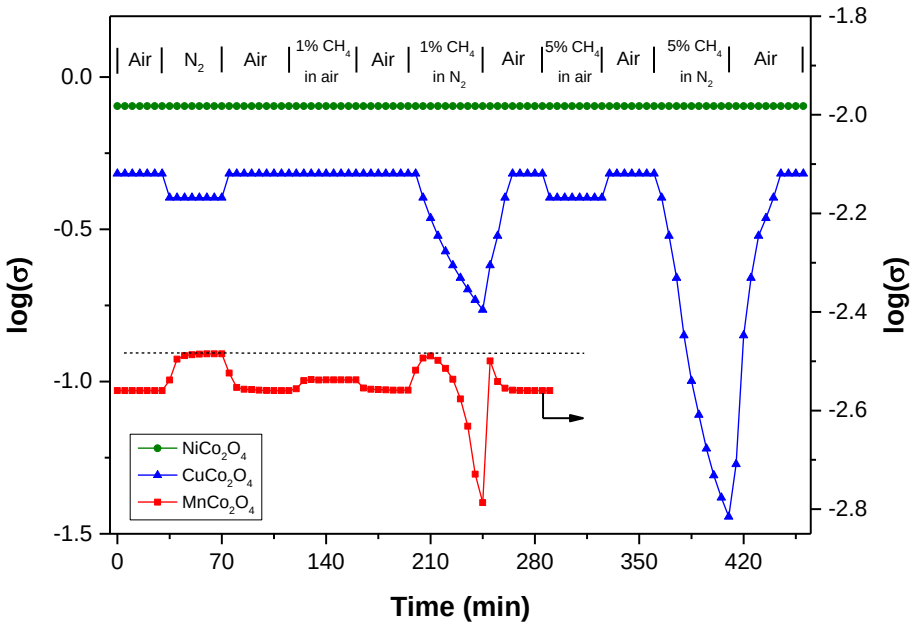

Figure 10. Variation of the electrical conductivity σ (in ohm^{-1} cm^{-1}) of the cobaltite-based materials during sequential exposures to different gaseous atmospheres at 350 °C.

No change of the electrical conductivity of the Ni cobaltite at constant temperature of 350 °C can be observed during sequences under different more or less reductive and oxidative gas mixtures, including 1 and 5 vol. % CH_4 in both air and nitrogen, suggesting that this mixed oxide does not have a redox behavior in these conditions, which include the catalytic reaction conditions. This clearly suggests that the oxidation of methane over the Ni cobaltite-based catalyst takes place via a reaction mechanism only involving chemisorbed oxygen species, i.e. a suprafacial reaction mechanism, a heterogeneous redox mechanism involving lattice oxygen species being firmly excluded. This behavior, already observed for a $LaCoO_3$ perovskite combustion catalyst [33], is obviously associated to its metallic conductivity state, the electrons from the delocalized σ*(e_g) band being likely involved in the surface bonding of reagents, i.e. methane and oxygen, and intermediates, which is correlated with a suprafacial reaction mechanism [66,67]. It is worth noting that the electrical behavior of the Ni cobaltite, which was shown to contain tiny amounts of NiO, is obviously governed by the $NiCo_2O_4$ phase. Indeed, NiO is known to be a p-type semiconducting oxide which is reversibly reduced with a hydrocarbon-air mixture [68]. Or this has not been observed with the Ni cobaltite sample, which remains in a metallic-like conductivity state whatever the nature of the gas phase in contact with the solid (Fig. 10), clearly suggesting that the $NiCo_2O_4$ phase is fully percolating and, thus, governs the electrical conductivity of this material.

For the Cu cobaltite, it can be observed that electrical conductivity decreased after the introduction of the nitrogen flow over the sample, suggesting its p-type character according to the Heckelsberg criterion [69], in line with the literature data for this spinel oxide [63]. When air was introduced again over the sample, the electrical conductivity reached quickly the initial value. Then a gaseous mixture containing 1 vol. % methane in air (the reaction mixture) was passed over the sample but, surprisingly, no change of the electrical conductivity could be observed. However, when the methane concentration in air was increased to 5 vol. %, the electrical conductivity decreased compared to that under air, confirming the p-type semiconducting character of Cu cobaltite. Moreover, when gas mixtures consisting of 1 and 5 vol. % methane in nitrogen flowed over the sample, the electrical conductivity strongly decreased, accounting for the reduction of the p-type oxide, which is greater when the concentration of the reducing gas (methane) is higher. For both methane concentrations in nitrogen the steady state cannot be reached after ca. 50 min, suggesting a slow diffusion of the oxygen vacancies formed on the surface of the solid into the bulk. Notably, when an air flow was passed over the reduced sample the electrical conductivity was completely restored suggesting that the reoxidation of the reduced solid was totally reversible. The reoxidation was immediate for the solid reduced under 5 vol. % methane in air, suggesting only a superficial reduction, while it took longer times, i.e. 20 and 35 min for the reduced solid under 1 and 5 vol. % methane in nitrogen, respectively, suggesting deeper bulk degrees of reduction. To conclude, the Cu cobaltite is a reducible p-type semiconducting oxide, which is, however, not reduced by the reaction mixture, i.e. 1 vol. % methane in air, at 350 °C, suggesting that, at least in these conditions, a suprafacial reaction mechanism is involved in the total oxidation of methane over this catalyst. This does not exclude the possibility of a heterogeneous redox mechanism operating at higher reaction temperatures over Cu cobaltite. Indeed, it has recently been shown that both suprafacial and intrafacial mechanisms can be involved separately or simultaneously in the total oxidation of methane over cube-shaped Co_3O_4 nanoparticles depending on the reaction temperature and the actual dioxygen pressure [70]. It is noteworthy that the electrical behavior of the Cu cobaltite, which was shown to contain a certain amount of CuO, is governed by the $CuCo_2O_4$ phase. Indeed, considering the well-known high reducibility of CuO, the reduction of Cu cobaltite sample under the reaction conditions would have been expected. Moreover, based on our previous results [36], CuO switches from p-type to n-type when reduced with hydrocarbon-air or hydrocarbon-nitrogen mixtures and the reoxidation of the reduced solid is not fully reversible. Or these phenomena have not been observed with the Cu cobaltite sample (Fig. 10), unambiguously suggesting that the $CuCo_2O_4$ phase is fully percolating and, thus, governs the electrical conductivity of this material.

In the case of Mn cobaltite, the electrical conductivity under nitrogen was higher than in air confirming its n-type character according to the Heckelsberg criterion [69]. Under air again, the electrical conductivity reached the initial value. Then, under the reaction mixture flow, i.e. 1 vol. % methane in air, the electrical conductivity slightly increased clearly suggesting the superficial reduction of the n-type oxide and, hence, the involvement of a heterogeneous redox mechanism in the total oxidation of methane over this catalyst. The reduced solid was completely reoxidized when air replaced the reaction mixture, accounting for the reversibility of the phenomenon. To get further information about the redox behavior of the $MnCo_2O_4$ spinel, a gaseous mixture containing 1 vol. % methane in nitrogen was then passed over the sample. It can be observed that the electrical conductivity first increased during ca. 15 min up to a maximum value not higher than that under pure nitrogen (dotted line on Fig. 10), in line with the n-type behavior of the solid, then, surprisingly, it strongly decreased during the next 35 min suggesting a switch to the p-type behavior. Finally, under a new air sequence the electrical conductivity first quickly jumped to a value close to the previously observed maximum and then decreased, as for an n-type oxide, reaching within ca. 15 min a plateau corresponding to the steady state in air which is identical with the initial plateau under air confirming the complete reoxidation of the $MnCo_2O_4$ spinel and, hence, the reversibility of the observed phenomena. To explain this behavior, it is worth remembering that, on one hand, in cobaltite spinels a $\sigma^*(e_g)$ band is formed by strong covalent B-O-B type interaction between the octahedral B-site cations [58], which are the dominant surface cations [71] and, on the other hand, in $MnCo_2O_4$ spinel, the tetrahedral A-sites are preferentially occupied by Co^{2+} cations, while the octahedral B-sites are occupied by mixed valence Co^{2+}, Co^{3+} (in low-spin state), Mn^{3+} and Mn^{4+} cations [72]. Among the octahedral B-site cations, only Co^{2+} has one electron on the e_g level, as it has the electronic configuration $t_{2g}^6 e_g^1$, being thus able to place charge carriers, i.e. electrons, in the $\sigma^*(e_g)$ band which are likely responsible for the n-type conductivity observed. However, these charge carriers are Anderson-localized [73] as demonstrated by the linear behavior of the $\ln(\rho)$ vs. $T^{1/4}$ plot for the $MnCo_2O_4$ sample within all the temperature range from 200 to 450 °C (Fig. S4), accounting for a semiconducting behavior associated to the hopping of electrons between Co^{2+} and Co^{3+} species on octahedral sites rather than a metallic behavior with itinerant electrons in the $\sigma^*(e_g)$ band as observed for $NiCo_2O_4$ sample. When methane is in contact with the $MnCo_2O_4$ sample, the octahedral Co^{3+} species are reduced to Co^{2+} leading to an increased charge carriers concentration and, hence, to an increased n-type electrical conductivity. However, this increase is limited, as observed in Fig. 10, due to a limited number of octahedral Co^{3+} species to be reduced to Co^{2+}. Under the reaction mixture, i.e. 1 vol. % methane in air, the solid remains of n-type, its reduction being obviously limited to the $Co^{3+} \rightarrow Co^{2+}$ reduction process, according to the following equation:

$$8Co_{Co}^{\times} + 4O_O^{\times} + CH_4 \rightarrow 8Co'_{Co} + 4V_O^{\bullet\bullet} + CO_2 + 2H_2O \quad (8)$$

where $Co_{Co}^{\times}$ and Co'_{Co} stand for Co^{3+} and Co^{2+} species, respectively, sitting on Co^{3+} octahedral lattice points. This leads to the conclusion that octahedral Co^{3+} species represent the catalytic site for the total oxidation of methane over $MnCo_2O_4$ spinel in the given reaction conditions which functions via a heterogeneous redox mechanism. On the other hand, under the methane-nitrogen mixture the reduction of all octahedral Co^{3+} to Co^{2+} species takes place first, the n-type electrical conductivity passing first through a maximum corresponding to an optimum Co^{3+}/Co^{2+} ratio in the octahedral sites, and then, when all the Co^{3+} species are reduced to Co^{2+}, it disappears. Continuing to expose the solid to the methane-nitrogen mixture, the solid continues losing oxygen with formation of oxygen vacancies but, now, with the simultaneous reduction of Mn^{4+} species on octahedral sites to Mn^{3+}, according to the following equation:

$$8Mn_{Co}^{\bullet} + 4O_O^{\times} + CH_4 \rightarrow 8Mn_{Co}^{\times} + 4V_O^{\bullet\bullet} + CO_2 + 2H_2O \quad (9)$$

where $Mn_{Co}^{\bullet}$ and $Mn_{Co}^{\times}$ stand for Mn^{4+} and Mn^{3+} species, respectively, sitting on Co^{3+} octahedral lattice points. As the conduction mechanism associated to the Mn^{4+}/Mn^{3+} polaron hopping is likely of p-type, i.e. electron hole hopping [74], this explains the observed switch from n-type to p-type of the $MnCo_2O_4$ spinel under the methane-nitrogen mixture (Fig. 10), while the reduction of Mn^{4+} species accounts for the observed decrease of the p-type conductivity. These phenomena are successively reversible when the solid is exposed to an air flow, the oxygen vacancies being filled in according to the following equations:

$$8Mn_{Co}^{\times} + 4V_O^{\bullet\bullet} + 2O_2 \rightarrow 8Mn_{Co}^{\bullet} + 4O_O^{\times} \quad (10)$$

$$8Co'_{Co} + 4V_O^{\bullet\bullet} + 2O_2 \rightarrow 8Co_{Co}^{\times} + 4O_O^{\times} \quad (11)$$

These results explain why $MnCo_2O_4$ spinel, which participates to the catalytic process with nucleophilic lattice O^{2-} species via a heterogeneous redox mechanism, is less active in the total oxidation reaction than $NiCo_2O_4$ and $CuCo_2O_4$ spinels, which are functioning via a suprafacial mechanism involving more reactive electrophilic adsorbed O_2^- and O^- species [65]. This is in line with the different nature of the active sites in $MnCo_2O_4$ spinel compared to $NiCo_2O_4$ and $CuCo_2O_4$ spinels, as suggested by the apparent activation energies (Table 3) and discussed in Section 3.2. On the other hand, as the latter spinels contain similar active sites, the remarkably higher intrinsic activity of $CuCo_2O_4$ compared to $NiCo_2O_4$ can be attributed to its significantly higher density of active sites (Section 3.2). Indeed, if the charge carriers are involved in the surface bonding of reagents and intermediates, as stated above for a suprafacial mechanism, then this is consistent with the appreciably greater charge carrier concentration estimated for $CuCo_2O_4$ spinel (Table 4). Finally, it should be pointed out that if an oxide is reduced under hydrogen and

reoxidized under oxygen during H_2-TPR and subsequent O_2-TPO experiments, respectively, within the reaction temperature range, this not necessarily demonstrates that it is reducible and functions via a heterogeneous redox mechanism under the reaction conditions.

4. Conclusions

Spinel-structured $MnCo_2O_4$, $NiCo_2O_4$ and $CuCo_2O_4$ were synthesized via coprecipitation followed by calcination at 450 °C. While Mn cobaltite consisted of a pure spinel phase, Ni and Cu cobaltites contain besides the spinel phase certain amounts of NiO and CuO side phases, respectively. Their surface area varies within a relatively wide range, from 30 $m^2\ g^{-1}$ for $CuCo_2O_4$ to 121 $m^2\ g^{-1}$ for $MnCo_2O_4$, following the inverse variation of the spinel phase crystallite size. All the cobaltites are reducible under hydrogen, the Ni and Cu cobaltites being completely reduced, while the degree of reduction of Mn cobaltite is limited to 88.4 %. All three samples also show high reoxidation abilities under oxygen. Their activity in the total oxidation of methane in terms of both T_{10} and intrinsic reaction rates, follows the order: Cu cobaltite > Ni cobaltite > Mn cobaltite. Mn and Cu cobaltites behave as semiconductors of n-type and p-type, respectively, while the Ni cobaltite is in a metallic conductivity state within all the temperature range studied. At constant temperature of 350 °C, which is in the kinetic domain for all the catalysts, $NiCo_2O_4$ and $CuCo_2O_4$ are not reduced under the reaction mixture, i.e. 1 vol. % methane in air, in spite of their high reduction and reoxidation abilities evidenced by H_2-TPR and O_2-TPO experiments, respectively. This clearly suggests that a suprafacial mechanism is operating during the oxidation of methane over these catalysts. At the same time, $MnCo_2O_4$ is reduced in the reaction conditions indicating that, in this case, a heterogeneous redox mechanism is involved.

Authors contribution

Marius-Alexandru Mihai: Investigation (catalysts preparation, catalytic tests, electrical conductivity measurements), Writing – original draft. **Daniela Cristina Culita:** Investigation (textural analysis). **Irina Atkinson:** Investigation (XRD analysis). **Florica Papa:** Investigation (H_2-TPR and O_2-TPO measurements). **Ionel Popescu:** Investigation (catalytic tests, electrical conductivity measurements), Methodology, Validation. **Ioan-Cezar Marcu:** Conceptualization, Methodology, Resources, Writing - review & editing, Supervision.

Declaration of Competing Interest

The authors declare that they have no known competing financial interests or personal relationships that could have appeared to influence the work reported in this paper.

Acknowledgments

The authors are grateful to Mr. Gabriel Crăciun from National Institute for Research and Development in Microtechnologies, Bucharest, Romania, for performing the SEM-EDX measurements.

References

1. Kuśtrowski, P., Rokicińska, A., Kondratowicz, T. Abatement of volatile organic compounds emission as a target for various human activities including energy production, Adv. Inorg. Chem., 72 (2018), 385:419.

2. Salthammer, T., Mentese, S., Marutzky, R., Formaldehyde in the indoor environment, Chem. Rev., 110 (2010), 2536:2572.

3. Fan, Z., Zhang, Z., Fang, W., Yao, X., Zou, G., Shangguan, W., Low-temperature catalytic oxidation of formaldehyde over Co_3O_4 catalysts prepared using various precipitants, Chinese Journal of Catalysis, 37 (2016), 947:954.

4. Huang, Y., Ye, K., Li, H., Fan, W., Zhao, F., Zhang, Y., Ji, H., A highly durable catalyst based on $Co_xMn_{3-x}O_4$ nanosheets for low-temperature formaldehyde oxidation, Nano Research, 9 (2016), 3881:3892.

5. Trivedi, S., Prasad, R., Choice of precipitant and calcination temperature of precursor for synthesis of $NiCo_2O_4$ for control of CO–CH_4 emissions from CNG vehicles, Journal of Environmental Sciences, 65 (2018), 62:71.

6. Lim, T.H., Cho, S.J., Yang, H.S., Engelhard, M.H., Kim, D.H., Effect of Co/Ni ratios in cobalt nickel mixed oxide catalysts on methane combustion, Applied Catalysis A: General, 505 (2015), 62:69

7. Trivedi, S., and Prasad, R., Selection of cobaltite and effect of preparation method of $NiCo_2O_4$ for catalytic oxidation of CO–CH_4 mixture, Asia- Pac. J. Chem. Eng., 12 (2017), 440:453.

8. Vishnyakov, A.V., Gridasova, T.P., Chashchin, V.A., Rodina, K.V., Catalytic Properties of SnO_2–TiO_2 Compositions in Total Methane Oxidation, Kinet. Catal. 52 (2011), 733:738.

9. Keav, S., Matam, S. K., Ferri, D., Weidenkaff, A. Structured, Perovskite-Based Catalysts and Their Application as Three-Way Catalytic Converters—A Review, Catalysts, 4 (2014), 226:255.

10. Abu-Zied, B.M., Soliman, S.A., Abdellah, S.E., Enhanced direct N_2O decomposition over $Cu_xCo_{1-x}Co_2O_4$ ($0.0 \leq x \leq 1.0$) spinel-oxide catalysts, Journal of Industrial and Engineering Chemistry, 21 (2015), 814:821.

11. Bion, N., Can, F., Courtois, X., Duprez, D., Vedrine, J.C., Metal Oxides in Heterogeneous Catalysis, Elsevier, 2018, Chapter 6, Transition metal oxides for combustion and depollution processes, pp. 287-335.

12. Li, Z., He-jian, L., Xiu-feng, X., Catalytic decomposition of N_2O over Mg-Co composite oxides hydrothermally prepared by using carbon sphere as template, J Fuel Chem Technol, 46 (2018), 569:577.

13. Neeft, J.P.A., Makkee, M., Moulijn, J.A., Catalytic oxidation of carbon black — I. Activity of catalysts and classification of oxidation profiles, Fuel, 77 (1998) 111:119.

14. Wang, J., Yang, G., Cheng, L., Shin, E.W., Men, Y., Three-dimensionally ordered macroporous spinel type MCr_2O_4 (M = Co, Ni, Zn, Mn) catalysts with highly enhanced catalytic performance for soot combustion, Catal. Sci. Technol., 5 (2015), 4594:4601.

15. Soloviev, S.O., Kapran, A.Y., Kurylets, Y.P., Oxidation of diesel soot on binary oxide CuCr(Co)-based monoliths, Journal of Environmental Sciences, 28 (2015), 171:177.

16. Faure, B., Alphonse, P., Co–Mn-oxide spinel catalysts for CO and propane oxidation at mild temperature, Applied Catalysis B: Environmental, 180 (2016) 715:725.

17. Prasad, R., Sony, Singh, P., Low temperature complete combustion of a lean mixture of LPG emissions over cobaltite catalysts, Catal. Sci. Technol., 3 (2013), 3223:3233.

18. Zhang, Z., Fan, Z., Guo, H., Fang, W., Chen, M., Shangguan, W., Effect of A^{2+} and B^{3+} substitution for Cobalt on low-temperature catalytic removal of formaldehyde over spinel $A_xB_{3-x}O_4$ (A = Mg, Ni, Zn; B = Cr, Fe, Al), Catalysis Today, 332 (2018), 139:143.

19. Heck, R.M.; Farrauto, R.J., Gulati, S.T. Catalytic air pollution control: commercial technology, 3rd ed., John Wiley & Sons, Inc., Hoboken, New Jersey, 2009.

20. Védrine, J.C., Heterogeneous Catalysis on Metal Oxides, Catalysts 7 (2017), 341.

21. Li, W.B., Wang, J.X., Gong, H., Catalytic combustion of VOCs on non-noble metal catalysts, Catalysis Today, 148 (2009), 81:87.

22. Spivey, J.J., Complete catalytic oxidation of volatile organics, Ind. Eng. Chem. Res., 26 (1987), 2165:2180.

23. Zhu, J., Gao, Q., Mesoporous MCo_2O_4 (M = Cu, Mn and Ni) spinels: Structural replication, characterization and catalytic application in CO oxidation, Microporous and Mesoporous Materials, 124 (2009), 144:152.

24. Hosseini, S.A., Alvarez-Galvan, M.C., Fierro, J.L.G., Niaei, A., Salari, D., MCr_2O_4 (M=Co, Cu, and Zn) nanospinels for 2-propanol combustion: Correlation of structural properties with catalytic performance and stability, Ceramics International, 39 (2013), 9253:9261.

25. Urdă, A., Popescu, I., Marcu, I.-C., in: M. Piumetti and S. Bensaid (Eds.) Nanostructured Catalysts for Environmental Applications, Springer: Heidelberg, Germany (2020), Chapter 1. Nanocrystalline spinel catalysts for volatile organic compounds abatement, 64 pp, *in press*.

26. Sickafus, K.E., Wills J.M., Structure of Spinel, Journal of the American Ceramic Society, 82 (1999), 3279:3792.

27. Brongersma, H.H., Groenen, P.A.C., Jacobs J.-P., Materials Science Monographs, Elsevier, 1995, Chapter Application of low energy ion scattering to oxidic surfaces, pp. 113-182.

28. Jacobs, J.-P., Maltha, A., Reintjes, J.G.H., Drimal, J., Ponec, V., Brongersma, H.H, The Surface of Catalytically Active Spinels, Journal of Catal., 147 (1994), 294:300.

29. Lim, T.H., Park, S.B., Kim, J.M., Kim, D.H., Ordered mesoporous MCo_2O_4 (M=Cu, Zn and Ni) spinel catalysts with high catalytic performance for methane combustion, Journal of Molecular Catalysis A: Chemical, 426 Part A (2017), 68:74.

30. Pu, Z., Liu, Y., Zhou, H., Huang, W., Zheng, Y., Li, X., Catalytic combustion of lean methane at low temperature over ZrO_2-modified Co_3O_4 catalysts, Applied Surface Science, 422 (2017), 85:93.

31. Herrmann, J.M., in: B. Imelik, J.C. Védrine (Eds.), Catalyst Characterization, Physical Techniques for Solid Materials, Plenum Press, New York, 1994, Chapter 20. Applications of electrical conductivity measurements in heterogeneous catalysis, pp. 559-584.

32. Popescu, I., Săndulescu, I., Rédey, Á., Marcu, I.-C., Study of the Catalytic Activity–Semiconductive Properties Relationship For $BaTiO_3$ and $PbTiO_3$ Perovskites, Catalysts for Methane Combustion. Catalysis Letters. 141 (2011), 445:451.

33. Popescu, I., Wu, Y., Granger, P., Marcu, I.-C, An *in situ* electrical conductivity study of LaCoFe perovskite-based catalysts in correlation with the total oxidation of methane, Applied Catalysis A: General, 485 (2014), 20:27.

34. Popescu, I., Boudjemaa, A., Helaili, N., Bessekhouad, Y., Tudorache, M., Bachari, K., Marcu, I.-C., Study of the electrical and catalytic properties of spinels with $CuFe_{2-x}Mn_xO_4$ composition (x=0, 0.4, 0.8, 1.6 and 2), Applied Catalysis A: General, 504 (2015), 29:36.

35. Dziembaj, R., Molenda, M., Zaitz, M.M., Chmielarz, L., Furczoń, K., Correlation of electrical properties of nanometric copper-doped ceria materials ($Ce_{1-x}Cu_xO_{2-\delta}$) with their catalytic activity in incineration of VOCs, Solid State Ionics, 251 (2013), 18:22.

36. Popescu, I., Piumetti., M., Bensaid., S., Marcu, I.-C., Study of Ce–Cu mixed oxide catalysts by *in situ* electrical conductivity measurements, Physical Chemistry Chemical Physics, 19 (2017), 31929:31939.

37. Popescu, I., Martínez-Munuera, J.C., García-García, A., Marcu, I.-C. Insights into the relationship between the catalytic oxidation performances of Ce-Pr mixed oxides and their semiconductive and redox properties, Applied Catalysis A: General, 578 (2019), 30:39.

38. Popescu, I., Trotuş, I.-T, Marcu, I.-C., Study by electrical conductivity measurements of semiconductive and redox properties of ceria and phosphated ceria catalysts, Applied Catalysis B: Environmental, 128 (2012), 55:63.

39. Marcu, I.-C, Săndulescu, I., Schuuman, Y., Millet, J.-M.M, Mechanism of n-butane oxidative dehydrogenation over tetravalent pyrophosphates catalysts, Applied Catalysis A: General, 334 (2008), 207:216.

40. Millet. J.-M.M., Marcu. I.-C., Herrmann, J.-M., Study by electrical conductivity measurement of redox properties of vanadium antimonate and mixed vanadium and iron antimonite, Journal of Molecular Catalysis A: Chemical, 226 (2005), 111:117.

41. Bilde, J., Janke, C., Lorentz, C., Delichere, P., Popescu, I., Marcu, I.-C., Loridant, S., Brückner, A., Millet, J.-M.M., Molecular Level Insights into the Structure of Active Sites of VAlO Mixed Oxides in Propane Ammoxidation, Journal of Physical Chemistry C, 117 (2013), 22926:22938.

42. Herrmann, J.-M., Vernoux, P., Béré, K.E., Abon, M., In Situ Study of Redox and of p-Type Semiconducting Properties of Vanadyl Pyrophosphate and of V–P–O Catalysts during the Partial Oxidation of n-Butane to Maleic Anhydride, Journal of Catalysis, 167 (1997), 106:117.

43. Schüth, F., Hesse, M., Unger, K.K., Precipitation and Coprecipitation, Handbook of Heterogeneous Catalysis, 2nd ed., Wiley-VCH: Weinheim, 2008, pp. 100-119.

44. Holland, B.J., Hay, J.N., The thermal degradation of poly(vinyl alcohol), Polymer, 42 (2001), 6775:6783.

45. Klissurski, D.G., Uzunova, E.L., A comparative study of the thermal stability of nickel, copper and zinc spinel cobaltites, Thermochimica Acta, 189 (1991), 143:149.

46. Thommes, M., Kaneo, K., Neimark, A.V., Olivier, J.P., Rodriguez-Reinoso, F., Rouquerol, J., Sing., K.S.W., Physisorption of gases, with special reference to the evaluation of surface area and pore size distribution (IUPAC Technical Report), Pure Appl. Chem., 87(9-10) (2015), 1051:1069.

47. Zeng, J., Xie, H., Zhang, G., Cheng, X., Zhou, G., Jiang, Y., Facile synthesis of CuCo spinel composite oxides for toluene oxidation in air, Ceramics International, 46 (2020), 21542:21550.

48. Chen, C., Liu, L., Li, Y., Li, W., Zhou, L., Lan, Y., Li, Y., Insight into heterogeneous catalytic degradation of sulfamethazine by peroxymonosulfate activated with CuCo2O4 derived from bimetallic oxalate, Chemical Engineering Journal, 384 (2020), 123257.

49. Cai, X., Sun, W., Xu, C., Cai, L., Yang, J., Highly selective catalytic reduction of NO via SO_2/H_2O-tolerant spinel catalysts at low temperature, Environmental Science and Pollution Research, 23 (2016), 18609:18620.

50. Yang, Y., Zeng, D., Gu, L., Liu, B., Guo, F., Ren, Y., Hao, S., Support-induced morphology and content tailored $NiCo_2O_4$ nanostructures on temperature-dependent carbon nanofibers with enhanced pseudocapacitive performance, Electrochimica Acta, 286 (2018), 1:13.

51. Zhang, L., Shi, L., Huang, L., Zhang, J., Gao, R., Zhang, D., Rational Design of High-Performance $DeNO_x$ Catalysts Based on $Mn_xCo_{3-x}O_4$ Nanocages Derived from Metal-Organic Frameworks, ACS Catalysis, 4 (2014), 1753:1763.

52. Klissurski, D.G., Uzunova, E.L., Cation-deficient nano-dimensional particle size cobalt-manganese spinel mixed oxides, Applied Surface Science, 214 (2003), 370:374.

53. Luo, J.-Y., Meng, M., Li, X., Li, X.-G, Zha,. Y.-Q., Hu, T.-D., Xie, Y.-N., Zhang, J., Mesoporous Co_3O_4–CeO_2 and Pd/Co_3O_4–CeO_2 catalysts: Synthesis, characterization and mechanistic study of their catalytic properties for low-temperature CO oxidation, Journal of Catalysis, 254 (2008), 310:324.

54. Franken, T., Terreni, J., Borgschulte, A., Heel, A., Solid solutions in reductive environment – A case study on improved CO_2 hydrogenation to methane on cobalt based catalysts derived from ternary mixed metal oxides by modified reducibility, Journal of Catalysis, 382 (2020), 385:394.

55. Kaczmarczyk, J., Zasada, F., Janas, J., Indyka, P., Piskorz, W., Andrzej Kotarba, A., Sojka, S. Thermodynamic Stability, Redox Properties, and Reactivity of Mn_3O_4, Fe_3O_4, and Co_3O_4 Model Catalysts for N_2O Decomposition: Resolving the Origins of Steady Turnover, ACS Catalysis, 6 (2016), 1235:1246.

56. Bagnasco, G., Cammarano, C., Turco, M., Esposito, S., Aronne, A., Pasquale Pernice, P. TPR/TPO characterization of cobalt-silicon mixed oxide nanocomposites prepared by sol-gel, Thermochimica Acta, 471 (2008), 51:54.

57. Pavel, M., Layrac, G., Tichit, D., Marcu, I.-C. Comparison of Cu_xZnAlO mixed oxide catalysts derived from multicationic and hybrid LDH precursors for methane total oxidation. Appl. Catal. A: Gen., 477 (2014), 195:204.

58. Bitla, Y., Chin, Y.-Y., Lin J.-C., Van, C.N., Liu, R., Zhu, Y., Liu, H.-J., Zhan, Q., Lin, H.-J., Chen, C.-T., Chu, Y.-H., He, Q., Origin of metallic behavior in $NiCo_2O_4$ ferrimagnet. Sci Rep 5, 15201 (2015).

59. Appandairajan, N.K., Gopalakrishnan, J., A study of $Co_{3-x}Ni_xO_4$ ($0 \leq x \leq 1$) system, Proceedings of the Indian Academy of Sciences - Section A, Chemical Sciences, 87 (1978). 115-:120.

60. Szymczewska, D., Molin, S., Hendriksen, P.V., Jasinski, P., Microstructure and electrical properties of Fe,Cu substituted $(Co,Mn)_3O_4$ thin films, Crystals 7 (2017) 185;

61. Brylewski, T., Kruk, A., Bobruk, M., Adamczyk, A., Partyka, J., Rutkowski, P., Structure and electrical properties of Cu-doped Mn-Co-O spinel prepared via soft chemistry and its application in intermediate temperature solid oxide fuel cell interconnects, Journal of Power Sources, 333 (2016), 145:155.

62. Dulov, A.A., Abramova, L.A., Frankfurt, G.I., Golosman, E.Z., Lapidus, A.L., Sominskii, S.D., Yakerson, V.I., Phase analysis of the surface of supported copper-cobalt oxide catalysts by means of electrical conductivity thermal-vacuum curves, Bulletin of the Academy of Sciences of the USSR, Division of chemical science, 36 (1987), 1594:1597.

63. Chen, H.-Y., Chen, J.-H., Preparation of p-type $CuCo_2O_4$ thin films by sol-gel processing, Materials Letters, 188 (2017), 63:65.

64. Masi, A., Bellusci, M., McPhail, S.J., Padella, F., Reale, P., Hong, J.-E., Steinberger-Wilckens, R., Carlini, M., The effect of chemical composition on high temperature behaviour of Fe and Cu doped Mn-Co spinels, Ceramics International, 43 (2017), 2829:2835.

65. F.A. Kröger, The Chemistry of Imperfect Crystals, Nort-Holland, Amsterdam, 1974.

66. Gellings, P.J., Bouwmeester, H.J.M., Ion and mixed conducting oxides as catalysts, Catalysis Today, 12 (1992), 1:101.

67. Voorhoeve, R.J.H., Remeika, J.P., Trimble, L.E., Defect chemistry and catalysis in oxidation and reduction over perovskite-type oxides, Annals of New York Academy of Sciences, 272 (1976), 3:21.

68. Popescu, I., Skoufa, Z., Heracleous, E., Lemonidou, A.A., Marcu, I.C., A study by electrical conductivity measurements of semiconductive and redox properties of Nb-doped NiO catalysts in correlation with the oxidative dehydrogenation of ethane, Physical Chemistry Chemical Physics, 17 (2015), 8138:8147.

69. Heckelsberg, L.F., Clark, A., Bailey, G.C., Electrical conductivity and catalytic activity of zinc oxide, The Journal of Physical Chemistry, 60 (1956), 559:561.

70. Zasada, F., Gryboś, J., Hudy, C., Janas, J., Sojka, Z., Total oxidation of lean methane over cobalt spinel nanocubes – Mechanistic vistas gained from DFT modeling and catalytic isotopic investigations, Catalysis Today 354 (2020), 183:195.

71. Wachs, I.E., Routray, K., Catalysis science of bulk mixed oxides, ACS Catalysis 2, 2012, pp. 1235-1246.

72. Bordeneuve, H., Tenailleau, C., Guillemet-Fritsch, S., Smith, R., Suard, E., Rousset, A., Structural variations and cation distributions in $Mn_{3-x}Co_xO_4$ ($0 \leq x \leq 3$) dense ceramics using neutron diffraction data, Solid State Sciences 12 (2010), 379:386.

73. Mott, N.F., The metal-insulator transition in extrinsic semiconductors, Advances in Physics, 21 (1972), 785:823.

74. Dorris, S.E., Mason, T.O, Electrical properties and cation valencies in Mn_3O_4, Journal of the American Ceramic Society, 71 (1988), 379:385.